Inorganic Chemistry

ARTICLE

pubs.acs.org/IC

Direct Observation of Rare-Earth Ions in α-Sialon:Ce Phosphors

Fangfang Xu,*[,†,‡] Erwan Sourty,[§] Wei Shi,[§] Xinliang Mou,[‡] and Linlin Zhang[‡]

[†]State Key Laboratory of High Performance Ceramics and Superfine Microstructures and
[‡]Test and Analysis Center of Inorganic Materials, Shanghai Institute of Ceramics, 1295 Dingxi Road, 200050 Shanghai, China
[§]Micro-electronics Port, FEI China, 690 Bibo Road, 201203 Shanghai, China

Supporting Information

ABSTRACT: Doping structures of Ce^{3+} into the refractory α-sialon crystal lattice have been examined via an atom-resolved Cs-corrected scanning transmission electron microscope. The location and coordination of the rare-earth ions are well-defined through direct observation in conjunction with structural modeling and image simulation. The stability and solubility of Ce^{3+} ions could be remarkably enhanced via congregation into the planar defects formed by a 1/3 ⟨210⟩-type lattice displacement along with an inversion operation. The formation of cylindrical chambers near the defects is believed to provide effective structural relaxation upon doping of large rare-earth ions into the interstices in their neighborhoods. The as-revealed structural information could be useful for understanding the luminescence properties of the promising rare-earth doped sialon materials.

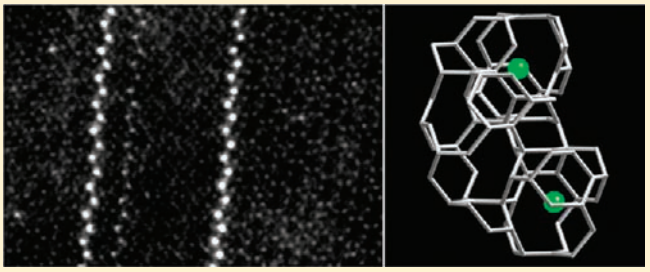

INTRODUCTION

α-Sialon is a solid solution isostructural with α-Si_3N_4 in which Si and N are partially replaced by Al and O, respectively. Such structure is metastable and is considered to be stabilized by incorporating metallic ions, such as lithium, magnesium, calcium, yttrium, or any of the lanthanides, in the large interstices in its structure. Thus, α-sialon, that is, α-Si-Al-O-N, is well established with the general formula $M_xSi_{12-m-n}Al_{m-n}O_nN_{16-n}$, where m is the number of Si−N bonds replaced by Al−N, n the number of Si−N bonds replaced by Al−O, and x equals m divided by the valence of the M cation.[1−5] α-Sialon exhibits high hardness, excellent high-temperature strength, and thermal shock resistance, which make it widely used in high performance ceramic materials.[6−10] Moreover, recent studies have indicated that lanthanide(Ln)-doped α-sialon materials have interesting luminescence properties, which suggest their potential application as novel phosphors with excellent thermal and chemical stabilities.[11−17] In addition, the α-sialon family shows the flexibility of varying the chemical composition over a wide range while maintaining the crystal structure, which favors the optimization and adjustment of luminescence properties. Because of the combined high-temperature and luminescence properties, α-sialon materials could be applied as electroluminescence materials or longer-lived phosphors under high-energy irradiation-like plasma display panels.

The structural or functional properties of α-sialon largely depend on the doped metals. For the doped Ln elements, the first-principles molecular-orbital calculations suggest that the Si(Al)-N(O) bonds are strengthened by the presence of a trivalent positive charge at the interstitial site of the α-sialon crystal. However, both Ln−N(O) and Ln−Si(Al) bonds are strongly antibonding, which becomes more significant when the ionic radius of Ln element increases.[18] The theoretical calculation has been well supported by the experimental results which show low solubility of larger Ln^{3+} in the α-sialon crystal lattice. Large ions, such as Ce^{3+} (r = 1.01 Å), have long been considered unable to be accommodated into the interstices, which have an average sphere radius of 1.46 Å. However, in the past decade several reports have been available in which the preparation of Ce-doped or even La-doped α-sialon (though the solubility was quite low), succeeded.[19−23] Meanwhile, the Ce-α-sialon has shown interesting luminescence property emitting green or blue light.[11−15] It is well-known that the emission of Ce^{3+} originates from a fully allowed transition from crystal-field component of the $5d^1$ state to the ground $4f^1$ state (i.e., 5d−4f transition). The interaction between the wave function of the electron in the 5d state, and the crystal field results in a broadening of this state and the splitting of the 5d energy level.[11−15,24] Therefore, for Ce^{3+} luminescence, the excitation usually has several peaks (≤5), and the emission consists of a broad band with two peaks in the long-wavelength ultraviolet region. The luminescence of Ce^{3+} depends on the host lattice. Compared to the oxides,[24] nitrogen-rich phase tend to show larger ligand-field splitting of the 5d band and center of gravity of the 5d states at lower energies because of the higher formal charge of N^{3-} compared with O^{2-} and the less electronegativity of nitrogen compared with oxygen (i.e., nephelauxetic effect).[11−15] These factors lead to the exceptional long-wavelength

Received: October 27, 2010
Published: March 03, 2011

emission of Ce-α-sialon. Therefore, the host crystal structure and specifically the location and coordination of rare-earth ions determine the luminescence properties of the Ln-doped phosphors.

So far, the exact location of large Ce^{3+} ions in α-sialon crystal has never been examined for two reasons. First, too few of doped Ce^{3+} ions made it impossible for structural refinement using X-ray diffractometry (XRD), and no effective facility was available at that moment to detect single atoms in the structure. The other is that people seem to be willing to accept the incorporation structure derived from light metal-doped α-sialon, for example, Ca, Mg, and Y, with comparatively high dopant concentration. XRD analysis then suggests that the metal ion locates at (1/3, 2/3, 3/8) or (2/3, 1/3, 7/8) inside the structural interstice and is coordinated with seven (N, O) anions.[25] On the other hand, previous work also observed some planar defects formed in the Ce-α-sialon crystals, which were proved to be related to the uneven distribution of Ce^{3+} ions.[26−29] However, the role of these structural defects still remain less clear. In the present study, we have taken advantages of newly developed atom-resolved Cs-corrected scanning transmission electron microscope (STEM) to examine the doping structures of Ce-α-sialon material. The precise location and coordination of Ce^{3+} ions could be directly determined. Therefore, the distribution, solubility and stability of Ln ions in the α-sialon crystal have been examined in detail by combining the atom-resolved imaging, structural modeling, and image simulation.

EXPERIMENTAL SECTION

Cerium-doped α-sialon material was prepared from a starting powder mixture of Si_3N_4 (SN-E10, Ube Industries Co., Tokyo, Japan), AlN (type F, Tokuyama Co., Tokyo, Japan), and 10 wt % CeO_2 (High Purity grade, Kanto Chemical Co., Tokyo, Japan). The starting composition was $13Si_3N_4$-9AlN-$2CeO_2$. One weight percent yttrium α-sialon seeds (SY-SY5, Ube Industries, Tokyo, Japan), with an average particle size of 0.2 μm, were added to the powder. The composition of the Y-α-sialon seeds is measured to have $m = 0.95$ and $n = 1.34$ in the general formula. The powder compacts were sintered by spark plasma sintering (SPS) at 1750 °C for 10 min, under a pressure of 30 MPa. Details of the preparation procedure were presented elsewhere.[22]

Atom-resolved structural observations were performed on a 300 kV Cs-corrected STEM (FEI Titan^{TM} 80−300) with a spatial resolution better than 0.1 nm. High-angle annular dark-field (HAADF) technique was applied to image individual Si(Al) and Ce atoms, which relies on the Z-contrast where the image intensity is approximately proportional to the square of atomic number.[30,31] To obtain reliable and convincible measurement of atomic positions, possible artifacts in imaging should be evaluated and eliminated as much as possible. The artifacts include image distortion resulting from, for instance, specimen drift or temperature fluctuations of the lens, and scanning noise resulting from, for instance, floor or acoustic vibrations, electro-magnetic interferences, various electronic instabilities from the acceleration voltage, emission, len and deflector current, detectors, etc. However, the Titan was designed to keep artifacts that commonly affect STEM imaging to a level not significant for resolutions up to one angstrom, provided the environment is suitable as for the instrument used in this work.[32,33] The sample for STEM observation was prepared via traditional processes including cutting, mechanical grinding, and polishing, ion-milling using Gatan PIPS, and finally coating with a thin carbon layer. Quantitative analysis of image contrast was carried out using DigitalMicrograph software. Models of doping structures were built using CrystalMaker software, according to which the image simulation was performed using MacTempas software.

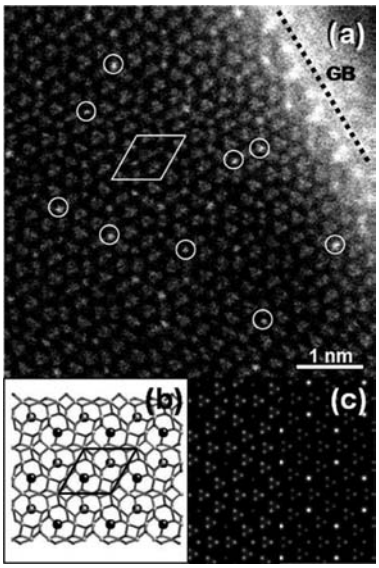

Figure 1. Structural analysis of α-sialon:Ce projected along the [001] direction. (a) HR-HAADF image of an α-sialon grain showing doping of Ce^{3+} ions with bright contrast part of which are marked by circles. GB represents the grain boundary. (b) The structural model of [001]-projected α-sialon where each of the interstices accommodates a Ce^{3+} ion at $x = 1/3$, $y = 2/3$ coordinates. (c) Calculated projected potential patterns in which the left-handed part represents the undoped α-sialon structure, while the right-handed part refers to the structure doped with Ce.

RESULTS AND DISCUSSION

α-Sialon has a trigonal $P31/c$ crystal structure and contains two large interstices in a $(Si,Al)_{12}(N,O)_{16}$ unit cell. The center of the interstitial holes locate at (1/3, 2/3, 1/4) and (2/3, 1/3, 3/4), respectively.[1−5] The metallic ions could be accommodated into these holes. For the smaller metals, like Li, Mg, Ca, Y, or a rare-earth metal with larger atomic number, comparatively higher amount of ions could be incorporated. Therefore structure refinement is possible and reveals that the metallic ion is coordinated with seven N(O) atoms and locates at (1/3, 2/3, 3/8) or (2/3, 1/3, 7/8).[25] It can be seen that the small metallic ions do not locate at the center of the interstices along c-dimension. However for the large doped ions like Ce^{3+}, broader space is required and the coordination situation must be different. Since structure refinement is impossible for such low doping content of extremely large ions, direct observation of individual atoms should be the only possible way to define their locations. Thanks to the newly developed Cs-corrected STEM, rare-earth atoms could be explicitly distinguished on a high-resolution (HR) HAADF image. Figure 1a shows the Z-contrast image of an α-sialon grain along the [001] zone axis. The bright dots, parts of which are marked by circles, refer to the Ce atom columns because the atomic number of Ce (58) is much larger than that of Si (14) or Al (13). The Si(Al) atoms appear as faint dots on the image. Figure 1b illustrates the [001]-projected structural model of α-sialon. The Ce^{3+} ions are assigned to the (x, y) coordinates of (1/3, 2/3) and (2/3, 1/3) in the unit cell. The corresponding calculated projected potential pattern is presented in Figure 1c (the right-handed part). The simulated image of α-sialon without rare-earth dopants

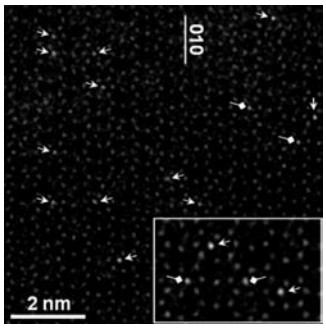

Figure 2. HR-HAADF image obtained along the [101] zone axis. The magnified image (inset) clearly shows the soybean-shaped pattern of Si(Al) atoms along with randomly accommodated Ce^{3+} ions appearing as bright dots (marked by arrows). The triangular arrows point to the Ce^{3+} ions locating closer to $z = 1/4$ while the rectangular arrows refer to those close to $z = 3/8$.

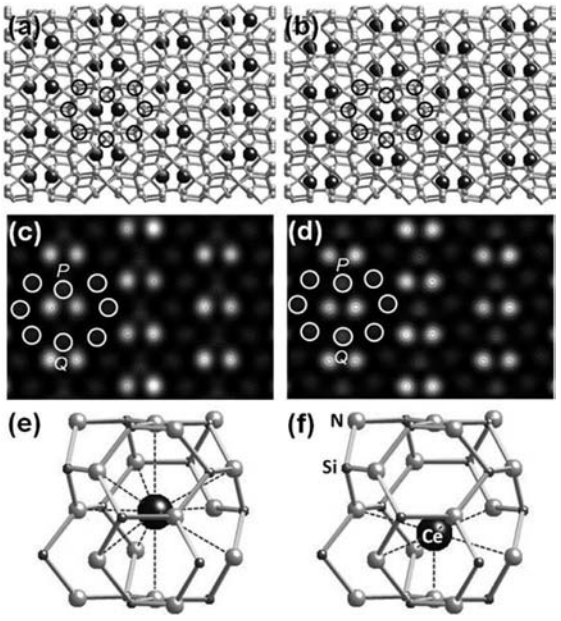

Figure 3. Determination of z-coordinate of Ce^{3+} in the structure. Panels a and b are the structural models viewed along [101] in which the location of Ce^{3+} is assigned to (1/3, 2/3, 1/4) and (1/3, 2/3, 3/8), respectively. Panels c and d are the simulated HAADF images according to the structural models in a and b, respectively. Panels e and f show the coordination condition of Ce^{3+} in an individual interstice with respect to a and b, respectively.

is also shown for comparison (see left-handed part of Figure 1c). The presence of Ce^{3+} ions apparently increases the intensity of dot contrast. The consistence between the calculated and experimental images indicates that Ce^{3+} ions locate at the center of the interstices with respect to the $x-y$ coordinate system.

To define the z-coordinate of Ce^{3+} ions, imaging along zone axes other than that parallel to c-axis is required. Therefore, the [101]-projected HR-HAADF image was acquired and is shown in Figure 2a. Again, sporadically distributed bright dots (marked by arrows) could be observed, which refer to the accommodation of Ce^{3+} ions in the structure. The reported z-coordinate of small doped metal ions is either 3/8 or 7/8 as seen in Figure 3f.[25] However, it is reasonable to consider that the large incorporated metal ions like Ce^{3+} require larger space and should locate much closer to the center of the interstices. Figure 3e illustrates the structural model where the Ce^{3+} ion locate at the center of the interstice, i.e. (1/3, 2/3, 1/4). In the [101] projection, the difference in z-coordinate of Ce^{3+} ions could be clearly revealed. Figure 3a illustrates the structural model of Ce-α-sialon viewing along [101] zone axis where the Ce^{3+} ions are assigned at the center of the interstices. Its calculated HAADF image is shown in Figure 3c. Similarly, the structural model and simulated image of [101]-projected crystal structure where Ce^{3+} ions locate at $z =$ 3/8 or 7/8 are presented in Figure 3b and 3d, respectively. The calculated images show apparent discrepancy owing to the modification of Ce locations particularly when we notice the position of Ce^{3+} ions (large bright dots) with respect to the Si(Al) atoms (faint dots) labeled with P and Q.

On a HR-HAADF image, the image intensity depends on the sum of atomic numbers along a certain atom column. Ce atoms appear brighter because of their high atomic number, while the difference in intensity for Si(Al) atom columns relies on the density of atoms at each projection position. N(O) atoms are too dim, and their contribution to the image intensity could be negligible. The α-sialon lattice exhibits soybean-shaped dot patterns on the [101]-projected HAADF image (Figure 2) if we filter out the faint contrast surrounding them. These dots refer to two Si(Al) atoms per unit length along the [101] direction as indicated by circles in the structural models in Figure 3a and b. By comparing the observed image (Figure 2) and the calculated images (Figure 3c and d) through measuring the positions of Ce^{3+} ions relative to those of Si(Al) labeled by P and Q, we can see that the z-coordinate of Ce^{3+} ions varies between 3/8 and 1/4 though majority of Ce^{3+} ions locate much closer to the center of the interstices. Twenty Ce^{3+}-ion locations have been measured and their z-values are illustrated in Supporting Information Figure S1. In Figure 2, the triangular and rectangular arrows point to the Ce^{3+} ions locating close to $z = 1/4$ and 3/8, respectively. The variation of z-coordinate for Ce^{3+} ions could be explained by the difference in local chemical environment dominated by the atom substitution in this solid solution. For $z = 1/4$, the Ce^{3+} ion is coordinated with eleven N(O) atoms in the interstice (see Figure 3e). According to the measured lattice parameters of the present Ce-α-sialon material, that is, $a = 7.95$ Å and $c = 5.69$ Å,[22] the Ce−N(O) bond length is approximately 2.845 (×2), 3.008 (×6), and 2.650 Å (×3), respectively. The bond length is somewhat larger than that in a seven-coordination configuration (see Figure 3f), that is, 2.744 (top 3), 2.744 (middle 3), and 2.134 Å (bottom 1). Since the majority of Ce^{3+} ions locate close to the center of the interstices, the increased coordination number, which is higher than 7, that is, around 9−11, must play an important role in the luminescence properties including crystal-field splitting, the center of gravity and the Stokes shift.

Though large rare-earth elements, like Ce, seem to be stabilized in the α-sialon crystal structure, the strong antibonding, as indicated by the theoretical calculation,[18] results in low solubility of Ce in the lattice. This has been evidenced by the present STEM observation which only detected sparsely distributed Ce^{3+} ions in the α-sialon crystallites. However, this situation could be remarkably changed via structural modulation. Our previous work has found that Ce^{3+} ions could be congregated into the planar defects formed via a 1/3 ⟨210⟩-type displacement.[28,29] The faults on different planes eventually enclose to form tetrahedron- or pyramid-shaped domains with the boundaries on some specific faces, that is, (001), {100}, and {101}. Structural modeling revealed generation of larger chambers at the

dx.doi.org/10.1021/ic102165g |*Inorg. Chem.* 2011, 50, 2905–2910

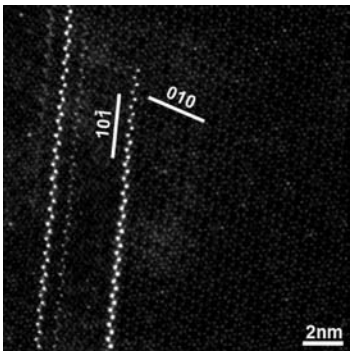

Figure 4. Observation of planar defects in α-sialon:Ce on a [101]-projected HR-HAADF image. Note the dense and periodic accommodation of rare-earth ions at the faults while loose distribution in the matrix lattice.

faulted area, which made us take for granted that these enlarged holes could accommodate more Ce^{3+} ions. However, the present atom-resolved imaging indicates that such assumption is wrong. Figure 4 shows the typical faults on $(10\bar{1})$ planes. By comparing the density and intensity of Ce^{3+} ions in the matrix lattice and the defect lattice, one can expect extremely high occupancy of Ce^{3+} ions at the interstitial sites near the faults especially when noting the periodic array of strong intensities. The present Z-contrast image is consistent to our previous chemical microanalysis via energy dispersive spectroscopy (EDS) in TEM, which also showed higher concentration of Ce at faulted area.[29]

Structural analysis using the diffraction contrast theory suggested that the faults in Ce-α-sialon were formed via a 1/3 ⟨210⟩-type displacement.[28] However, the present HR-HAADF imaging reveals an additional inversion operation involved. The magnified image in Figure 5a clearly shows inversion relationship between the soybean patterns on either side of the fault along with a 1/3 ⟨210⟩ lattice shift. According to the revealed defect structure, the structural model is established and illustrated in Figure 5b. Here, the Ce^{3+} ions are assigned at the center of interstices in the structural model. In Figure 5a, the array of black dots superimposed onto the bright spots refers to the array of Ce^{3+} ions (big dark balls in Figure 5b) at the fault plane in the structural model. Therefore, the structural model agrees well with the observed image. Apparently, the structural modification near the faults makes the large rare-earth ions more stable into the interstices. The α-sialon structure has a trigonal symmetry which is composed of two rows of interstices and one row of densely bonded Si(Al)−N(O) network along *c*-axis (see Figure 6a). The interstice consists of four atomic layers along *c*-axis, therefore the α-sialon structure is generally described as ABCD packing structure in comparison to the ABAB packing structure for *β*-sialon.[1−5] The 1/3 ⟨210⟩-type displacement, no matter an additional inversion operation is involved or not, makes the rows interchange at the fault plane. As a result, a cylindrical chamber composed of five atomic layers is formed near the fault plane (see arrowed region and the inset in Figure 6b). The sites marked by the ellipses on the fault plane in Figure 5b represent the positions of these elongated holes. Apparently, no Ce^{3+} ions have been observed at these sites on Figure 5a. The creation of cylindrical chambers does not aim to provide broader space for accommodation of large rare-earth ions as the coordination condition may not meet the stabilization of metal ions. In contrast, we believe that such hollow bonding network has effectively relax the lattice

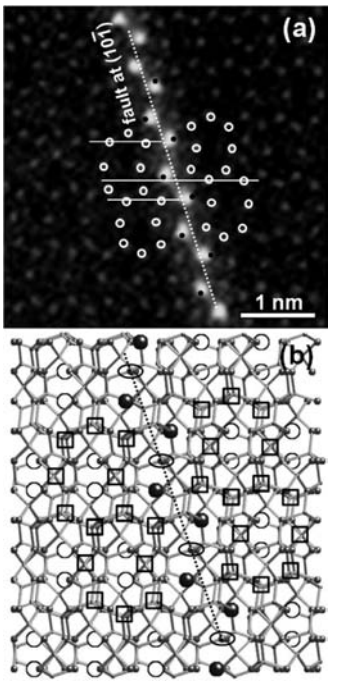

Figure 5. Structural analysis of the fault structure. (a) The magnified image showing a fault formed by a 1/3 ⟨210⟩-type lattice displacement along with an inversion operation. (b) The structural model of the fault. The large circles refer to the centers of the interstices where Ce^{3+} ions might reside and the squares outline the soybean-shaped Si(Al) sublattice. The sites marked by the ellipses represent the positions of cylindrical chambers formed on the fault plane.

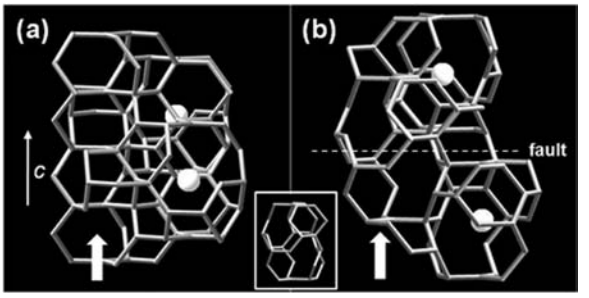

Figure 6. Models of interstitial configuration in the matrix lattice (a) and at the fault region (b). Note the generation of cylindrical chamber (inset) at the arrowed position after the lattice transition.

strains aroused from the normal interstices in its neighborhood where large Ce^{3+} ions are accommodated.

The interstice in the α-sialon structure resembles a roughly cylindrical shape rather than a spherical cage. The height (*H*) along *c*-axis is slightly larger than the diameter (*D*) in the cylinder. Incorporation of large metal ions should expand the interstice hence increase the structural parameters. But the increment scope differs for *a* and *c* parameters depending on the doped metal ions. As can be seen in Table 1, doping of Ce makes the unit cell expand more in both *a*- and *c*-dimension than that doped with smaller ions, for example, Y. In addition, the *c*/*a* ratio decreases in Ce-α-sialon suggesting broader expansion in *a*- than in *c*-dimension when larger metals are accommodated. As a result, the cylindrical interstice tends to be more like a sphere. Table 1 presents the values of diameter and height of the interstice in α-Si_3N_4 and

Table 1. Structural Parameters of α-Si_3N_4 and Its Solid Solutions[a]

	a (Å)	c (Å)	c/a	D (Å)	H (Å)	D/H	r_D (%)	r_H (%)
α-Si_3N_4	7.748	5.617	0.725	5.353	5.617	0.953		
Y-α-sialon[29] (x = 0.38)	7.805	5.687	0.729	5.394	5.687	0.948	0.77	1.25
Ce-α-sialon	7.95	5.69	0.715	5.488	5.69	0.964	2.52	1.30

[a] D = diameter of interstice; H = height of interstice in c-direction; $r_D = (D - D_{\alpha\text{-}Si_3N_4})/D_{\alpha\text{-}Si_3N_4}$; $r_H = (H - H_{\alpha\text{-}Si_3N_4})/H_{\alpha\text{-}Si_3N_4}$.

its solid solutions doped with different metals. Though the doping content is quite low, Ce-α-sialon already shows a considerable expansion of interstices in a-dimension, that is, 2.52% increment with respect to that in the α-Si_3N_4 structure. Since the XRD analysis usually gives a mean value of structural parameters, the actual size of interstice should be even larger at the site that a Ce^{3+} ion is accommodated. As a whole, because of $D/H < 1$ for the interstice, the demand of expansion in a-dimension is more critical than that in c-dimension. However, the row of stiff Si(Al)-N(O) network in the close vicinity of the rows of interstices (see arrowed region in Figure 6a) hinders the expansion of interstices required for doping of large metal ions. On the contrary, the created hollow chamber (see Figure 6b) near the fault after a lattice displacement makes the "walls" of interstices much softer, hence lowered strain energy involved in the accommodation of Ce^{3+} ions through some easy operations of chemical bonds within the chamber, for example, twist or rotation.

Though the sole 1/3 ⟨210⟩ lattice shift is enough to create cylindrical chambers,[28,29] an additional inversion operation is found prerequisite for lowering the strain energy at the faulted region. We compare the structural models with and without an inversion operation and find that the inversion operation can produce a more symmetrical structure where all the surrounding interstices could be effectively bounded with the hollow chamber, hence maximal relaxation of structural stains (see Supporting Information Figure S2).

Extensive atom-resolved STEM examinations of Ce-α-sialon crystallites through different viewing directions never observed simultaneous doping of Ce^{3+} ions in the neighboring interstices within the matrix lattice. In contrast, the array of highest intensity at the fault plane suggests both high occupancy and accommodation of metal ions in neighboring interstices. In the present study, we tried to estimate the occupancy of Ce at the faults by using multislice image simulation. However, since the fault we examined was a part of domain boundary, which should be a facet of either a tetrahedron or a pyramid, the actual size and shape of the fault can hardly be defined. Therefore, precise determination of Ce occupancy is impossible. Anyway, the measurement of intensity of dot contrast at Ce positions suggests that more than three times higher occupancy is achieved at faults than in the matrix lattice.

The present study indicates that the crystal structure could be tailored via introduction of defects aiming to stabilize the doped elements and increase the solubility of dopants. A quick synthetic process, for example, the spark plasma sintering used in the present preparation of Ce-α-sialon, seems to provide a dynamic driving force for the generation of metastable defect structures. In fact, the SPS technique has been widely used to synthesize many new ceramic materials in a nonequilibrium condition.[34−37] Therefore the doping structure and dopant concentration could be controlled via adjusting the synthetic conditions including powder composition, temperature, and sintering time, which finally reaches the end to optimize the corresponding physical properties of the doped materials. For applications in luminescence, usually as high as possible Ln ion concentration up to a few percent is desirable to obtain high luminescence intensity. However, some unwanted effects may arise including cross-relaxation, concentration quenching, etc. In the case of high dopant concentration, the luminescence ions become so close that the excitation energy starts to migrate among them and becomes progressively lost at unspecified nonradiative traps (lattice defects).[24,38] The concentration quenching is determined primarily by the dipole−dipole interaction between rare-earth ions, which weakens as R^{-6} with an increase in the distance between the ions. There exists a critical value R_c, below which the luminescence is completely quenched. Generally for concentration quenching, the effective radius of the dipole−dipole interaction between rare-earth ions is approximately equal to 0.3−0.5 nm.[39,40] In α-sialon crystal structure, the shortest Ce−Ce distance, that is, the span of two neighboring interstices is around 0.53−0.57 nm,[41] which is just beyond the critical value for concentration quenching. The correlation between the high-amount doping in faults and the luminescence property is being investigated by combining TEM and SEM-CL (cathodoluminescence) techniques and will be reported in the near future. Anyway, a recent study has shown that the Eu^{2+} ions could be accommodated at stacking faults in AlN, which is called a defect phosphor showing high luminescence.[42]

CONCLUSIONS

An atom-resolved Cs-corrected scanning transmission microscope has been used to analyze the doping structures of the α-sialon:Ce material which has excellent high-temperature mechanical and promising luminescence properties. The location of doped Ce^{3+} ions has been well-defined and is found to be majorly close to the center of large interstices in the α-sialon crystal structure, hence the coordination number larger than seven, that is, 9−11. However, the solubility of Ce is quite low in the matrix lattice which is consistent to the previous theoretical consideration indicating strong antibonding between N(O) and rare-earth ions especially when the diameter of metal ions is very large. Such condition could be remarkably changed as revealed by the present structural analysis. A planar defect formed by a 1/3 ⟨210⟩-type lattice displacement along with an inversion operation generates a cylindrical chamber, which can effectively relax the lattice strains aroused from the neighboring interstices where comparatively large amount of Ce^{3+} ions are accommodated. The present study suggests that the doping structure could be tailored via certain lattice operations, which may make it possible to control the dopant concentration and hence the adjustment of physical properties.

ASSOCIATED CONTENT

Supporting Information. The z-coordinates of Ce^{3+} ions measured from twenty cerium sites; Schematic explanation of

dx.doi.org/10.1021/ic102165g |Inorg. Chem. 2011, 50, 2905–2910

why an inversion operation is prerequisite in the formation of faults. This material is available free of charge via the Internet at http://pubs.acs.org.

AUTHOR INFORMATION

Corresponding Author

*Address: Shanghai Institute of Ceramics, 1295 Dingxi Road, 200050 Shanghai, China. Tel: +86-21-52412574. Fax: +86-21-52415615. E-mail: ffxu@mail.sic.ac.cn.

ACKNOWLEDGMENT

This work was supported by the SICCAS Innovation Program and the 973 programs (Grant No. 2007CB936704, 2009CB939904).

REFERENCES

(1) Mitomo, M. *Yogyo-Kyokaishi* **1977**, *85*, 50.
(2) Hampshire, S.; Park, H. K.; Thompson, D. P.; Jack, K. H. *Nature* **1978**, *274*, 880–883.
(3) Hwang, Z. K.; Tien, T. Y.; Yen, T.-S. *J. Am. Ceram. Soc.* **1986**, *69*, C-241–C-242.
(4) Cao, G. Z.; Metselaar, R. *Chem. Mater.* **1991**, *3*, 242–252.
(5) Ekström, T.; Nygren, M. *J. Am. Ceram. Soc.* **1992**, *75*, 259–276.
(6) Chen, I. W.; Rosenflanz, A. *Nature* **1997**, *389*, 701–704.
(7) Nordberg, L. O.; Nygren, M.; Kall, P. O.; Shen, Z. J. *J. Am. Ceram. Soc.* **1998**, *81*, 1461–1470.
(8) Pettersson, P.; Shen, Z. J.; Johnsson, M.; Nygren, M. *J. Eur. Ceram. Soc.* **2001**, *21*, 999–1005.
(9) Shen, Z. J.; Zhao, Z.; Peng, H.; Nygren, M. *Nature* **2002**, *417*, 266–269.
(10) Shuba, R.; Chen, I. W. *J. Am. Ceram. Soc.* **2006**, *89*, 2147–2153.
(11) van Krevel, J. W. H.; Hintzen, H. T.; Metselaar, R.; Meijerink, A. *J. Alloys Compd.* **1998**, *268*, 272.
(12) van Krevel, J. W. H.; Hintzen, H. T.; Metselaar, R. *Mater. Res. Bull.* **2000**, *35*, 747.
(13) van Krevel, J. W. H.; van Rutten, J. W. T.; Mandal, H.; Hintzen, H. T.; Metselaar, R. *J. Solid State Chem.* **2002**, *165*, 19–24.
(14) Xie, R. J.; Mitomo, M.; Uheda, K.; Xu, F. F.; Akimune, Y. *J. Am. Ceram. Soc.* **2002**, *85*, 1229–1234.
(15) Xie, R. J.; Hirosaki, N.; Mitomo, M.; Yamamoto, Y.; Suehiro, T.; Ohashi, N. *J. Am. Ceram. Soc.* **2004**, *87*, 1368–1370.
(16) Xie, R. J.; Hirosaki, N.; Mitomo, M.; Yamamoto, Y.; Suehiro, T.; Sakuma, K. *J. Phys. Chem. B* **2004**, *108*, 12027–12031.
(17) Xie, R. J.; Hirosaki, N.; Mitomo, M.; Takahashi, K.; Sakuma, K. *Appl. Phys. Lett.* **2006**, *88*, 101104.
(18) Nakayasu, T.; Yamada, T.; Tanaka, I.; Adachi, H. *J. Am. Ceram. Soc.* **1996**, *79*, 2527–2532.
(19) Ekström, T.; Nygren, M.; Käll, P.-O.; Olsson, P.-O. *J. Mater. Sci.* **1989**, *24*, 1853–1861.
(20) Mandal, H.; Thompson, D. P. *J. Mater. Sci. Lett.* **1996**, *15*, 1435–1438.
(21) Mandal, H. *J. Eur. Ceram. Soc.* **1999**, *19*, 2349–2357.
(22) Wang, C. M.; Mitomo, M.; Xu, F. F.; Hirosaki, N.; Bando, Y. *J. Am. Ceram. Soc.* **2001**, *84*, 1389–1391.
(23) Shuba, R.; Chen, I. W. *J. Am. Ceram. Soc.* **2006**, *89*, 2860–2868.
(24) Blasse, G.; Grabmaier, B. C. *Luminescent Materials*; Springer Verlag: Berlin, 1994.
(25) Izumi, F.; Mitomo, M.; Suzuki, J. *J. Mater. Sci. Lett.* **1982**, *1*, 533–535.
(26) Olsson, P.-O. *J. Mater. Sci.* **1989**, *24*, 3878–3887.
(27) Ekström, T.; Jansson, K.; Olsson, P.-O.; Persson, J. *J. Eur. Ceram. Soc.* **1991**, *8*, 3–9.
(28) Xu, F. F.; Wang, C. M.; Bando, Y.; Mitomo, M.; Kurashima, K. *Philos. Mag. A* **2001**, *81*, 2271–2284.
(29) Xu, F. F.; Bando, Y.; Wang, C. M.; Mitomo, M. *J. Am. Ceram. Soc.* **2002**, *85*, 466–472.
(30) Pennycook, S. J.; Boatner, L. A. *Nature* **1988**, *336*, 565–567.
(31) Spence, J. C. H. *High-Resolution Transmission Electron Microscopy*; Oxford University Press: Oxford, U.K., 2003.
(32) van der Stam, M.; Stekelenburg, M.; Freitag, B.; Hubert, D.; Ringnalda, J. *Microsc. Anal.* **2005**, *19*, 9–11.
(33) Muller, D. A.; Grazul, J. *J. Electron Microsc.* **2001**, *50*, 219–226.
(34) Mitomo, M.; Ishida, A. *J. Eur. Ceram. Soc.* **1999**, *19*, 7–15.
(35) Molenat, G.; Thomas, M.; Galy, J.; Couret, A. *Adv. Eng. Mater.* **2007**, *9*, 667–669.
(36) Qi, X.; Bao, Q. L.; Li, C. M.; Gan, Y.; Song, Q. L.; Pan, C. X.; Tang, D. Y. *Appl. Phys. Lett.* **2008**, *92*, 113113.
(37) Fu, Y. Q.; Shearwood, C.; Xu, B.; Yu, L. G.; Khor, K. A. *Nanotechnology* **2010**, *21*, 115707.
(38) Powell, R. C.; Blasse, G. *Struct. Bonding (Berlin)* **1980**, *42*, 44–96.
(39) Weber, H. P.; Damen, T. C.; Danielmeyer, H. G.; Tofield, B. C. *Appl. Phys. Lett.* **1973**, *22*, 534–536.
(40) Singh, S.; Miller, D. C.; Potopowicz, J. R.; Shick, L. K. *J. Appl. Phys.* **1975**, *46*, 1191–1196.
(41) Xu, F. F.; Zhang, L. L.; Du, X. F.; Zhu, Y. C. *Cryst. Growth Des.* **2008**, *8*, 2574–2580.
(42) Takeda, T.; Hirosaki, N.; Xie, R. J.; Kimoto, K.; Saito, M. *J. Mater. Chem.* **2010**, *20*, 9948–9953.